



Ru-Ru₂P hetero-cluster promoted V₂CT_x sheets-based electrocatalyst enables industrial-level AEM water electrolysis

Thanh Hai Nguyen^a, Phan Khanh Linh Tran^a, Duy Thanh Tran^{a,*}, Van An Dinh^b,
Nam Hoon Kim^a, Joong Hee Lee^{a,c,**}

^a Department of Nano Convergence Engineering, Jeonbuk National University, Jeonju, Jeonbuk 54896, the Republic of Korea

^b Department of Precision Engineering, Graduate School of Engineering, Osaka University, 2-1, Yamada-oka, Suita, Osaka 565-0871, Japan

^c Carbon Composite Research Center, Department of Polymer-Nano Science and Technology, Jeonbuk National University, Jeonju, Jeonbuk 54896, the Republic of Korea

ARTICLE INFO

Keywords:

Ru–Ru₂P hetero-clusters
V₂CT_x MXene sheets
PH–universal hydrogen evolution reaction
AEM water electrolyzer

ABSTRACT

Water electrolysis is a remarkably advantageous technology for producing green hydrogen energy to substitute fossil fuels; however, the design of high-performance electrocatalysts with affordable prices and fast reaction kinetics is still a great challenge. Herein, we report well-dispersed ruthenium–ruthenium phosphide hetero-clusters stabilized vanadium carbide nanosheets (Ru–Ru₂P/V₂CT_x) as an outstanding catalyst for pH–universal hydrogen evolution reaction. The Ru–Ru₂P/V₂CT_x requires low overpotentials of 37, 21, and 95 mV to reach 10 mA·cm^{−2} in 0.5 M H₂SO₄, 1.0 M KOH, and 1.0 M PBS, respectively. Theoretical calculations well manifest the underlying structure–performance relationship of catalyst and mechanism for superb activity. The stack of anion exchange membrane water electrolyzer single cell achieves 1.0/2.0 A·cm^{−2} at 1.80/2.05 V at 60 °C, along with exceptional durability over 550 h continuous operation. These findings provide new insights into the development of efficient catalysts for water electrolyzers, ex. AEMWEs, in practical large-scale green hydrogen production.

1. Introduction

Electrochemical water splitting is an attractive zero-emission approach to producing high-purity H₂ for sustainable and clean energy conversion. The low-temperature water electrolysis, ex. anion exchange membrane water electrolyzer (AEMWE), has been investigated in recent years due to the significant benefits it offers of low-cost hardware together with less corrosive environments and impressive performance (typically reaching 1–2 A·cm^{−2}) [1,2]. However, the efficiency is still unsatisfactory from the high overpotentials and poor durability at the cathode caused by the hydrogen evolution reaction (HER) [3]. Therefore, an efficient and durable HER electrocatalyst is urgently needed to yield H₂ in industrial-scale implementation. Precious commercial catalysts based on Pt, Rh, and Ir are considered state-of-the-art HER electrocatalysts in light of their outstanding performance [4,5]; however, their high cost and scarcity have greatly limited their widespread utilization [6]. Meanwhile, ruthenium (Ru) owns a favorable H₂ bonding strength and is economically cost-effective (~ 1/2 price as compared to

Pt), hence the recently reported Ru-based electrocatalysts have been emerging as a replacement to expensive precious metal groups for pH-universal HER catalysis [7–9]. Unfortunately, the significant drawbacks of particle agglomeration during the preparation and reaction processes caused by high surface energy and strong interatomic metallic bonds underestimate their remarkable performance [10,11]. In addition, although nanocarbons and their derivatives have been widely adopted to provide the flexible structure to ensure the support/immobilization of catalyst nanoparticles (NPs) [12,13], the weak guest–host interactions cannot avoid metal aggregates, thus inhibiting active sites, and then lowering the electrochemical activities [10,14].

MXene, a 2D emerging star, has garnered widespread attention thanks to its exceptional electrochemical conductivity, robust structural stability, and high specific surface area [15]. There has been tremendous literature on MXene-based materials in widespread applications, especially in energy storage [16,17] and electrocatalysis [18,19]. Among the MXene family, V₂CT_x has been receiving much attention for its electrochemistry prospects due to the lower atomic layers per MXene sheet,

* Corresponding author.

** Corresponding author at: Department of Nano Convergence Engineering, Jeonbuk National University, Jeonju, Jeonbuk 54896, the Republic of Korea.

E-mail addresses: dttran@jbnu.ac.kr (D.T. Tran), jhl@jbnu.ac.kr (J.H. Lee).

<https://doi.org/10.1016/j.apcatb.2023.123517>

Received 29 August 2023; Received in revised form 3 November 2023; Accepted 12 November 2023

Available online 15 November 2023

0926-3373/© 2023 Elsevier B.V. All rights reserved.

resulting in a larger surface area with rich active centers [20]. Considering the multiple oxidation states of vanadium and abundant surface terminations, V_2CT_x could potentially enable the strong active catalyst-support interaction to construct hybrid material, ensuring the uniform dispersion of active catalysts on the MXene surface [21,22]. Additionally, the strong active catalyst-support interaction can induce electronic redistribution to improve the electron transfer ability and stability [23,24]. Of note, the development of MXene-based advanced electrocatalysts is in its infancy, with major efforts focusing on the $Ti_3C_2T_x$ [25–27]. To the best of our knowledge, the vanadium-based MXene electrocatalysts have rarely been reported [28–30]. Therefore, there is high motivation to experimentally and theoretically explore V_2CT_x for the development of efficient HER electrocatalysts to power water electrolysis.

In this work, we successfully immobilize high-density Ru–Ru₂P hetero-clusters on V_2CT_x nanosheets (Ru–Ru₂P/ V_2CT_x) by a convenient process. The strong active catalyst-support interaction could be formed through Ru–O–V bonds to secure the good dispersion and stability of Ru–Ru₂P clusters. Theoretical calculation proves that the synergistic effect between Ru–Ru₂P/ V_2CT_x could lead to electronic reconfiguration and effectively tailor the d-band center of Ru sites at Ru–Ru₂P interface to achieve low energy barrier of water dissociation as well as favored free energy of hydrogen adsorption/desorption, thus resulting in impressive HER performances in 0.5 M H₂SO₄, 1.0 M KOH, and 1.0 M PBS, outperforming the most recent literatures on Ru/MXene-based catalysts. Further investigation of an AEMWE stack derived from the Ru–Ru₂P/ V_2CT_x HER catalyst reveals small cell voltages of 1.80/2.05 V to reach 1.0/2.0 A cm^{−2} along with stable operation, evidencing its high potential for industrial water splitting application.

2. Experimental section

2.1. Materials

All the chemicals and reagents were used directly, without further purification. The V_2AlC MAX phase (400 mesh) was provided by the Laizhou Kai Kai Ceramic Materials Co., Ltd. (China). Sulfuric acid (H₂SO₄, 95.0 – 98.0 %), hydrofluoric acid (HF, 48 %), ruthenium (III) chloride hydrate (RuCl₃·xH₂O), tetrabutylammonium hydroxide solution [(CH₃CH₂CH₂CH₂)₄N(OH), 54.0 – 56.0 % in H₂O], platinum on graphitized carbon (20 wt% loading), ruthenium(IV) oxide (99.9 %), sodium phosphate monobasic (NaH₂PO₄, 99.0%), sodium phosphate dibasic (Na₂HPO₄, 99.0 %), and sodium hypophosphite monohydrate (NaH₂PO₂·H₂O, 99.0 %) were obtained from Sigma–Aldrich. Samchun Chemical Co. (Korea) provided potassium hydroxide (KOH, pellets, 85.0 %) and isopropyl alcohol [IPA, (CH₃)₂CHOH, 99.0 %].

2.2. Synthesis of exfoliated V_2CT_x nanosheets

The V_2AlC powders were etched via the modified HF etching route, which was reported elsewhere [20,29]. Typically, 1.0 g of V_2AlC was slowly added into 20 mL of 48.0 % HF under vigorous stirring at 40 °C for 48 h. Then, the etching V_2AlC was centrifuged with plentiful deionized ion (DI) water until the pH reached ~7, and eventually obtained by a freeze-drying process. To obtain a few layers of V_2CT_x MXene, 0.5 g of etching V_2AlC powders was placed into 10 mL of concentrated TBAOH solution with continuous stirring for 24 h. Afterward, the supernatant was washed to eliminate the residual TBAOH. After centrifugation, 200 mL of DI water was added to the remaining clay, and this was exfoliated by ultra-sonication for 1 h under an iced bath. Then, the delaminated V_2CT_x MXene suspension was collected by centrifugation at 3 500 rpm for 30 min to separate the heavier particles. Finally, the obtained suspension was quickly frozen in liquid N₂ and freeze-dried for at least 4 days in iLShinBioBase Freeze Dryer with the condenser temperature of − 85 °C and vacuum pressure of less than 10 mTorr. The obtained product was termed V_2CT_x MXene.

2.3. Synthesis of Ru–Ru₂P/ V_2CT_x hybrid material

First, 25 mg of V_2CT_x was added into 50 mL of DI water, to which sonication was then applied to obtain a stable V_2CT_x suspension (2 mg·mL^{−1}). Then, 10 mL of 3 mg·mL^{−1} RuCl₃ was poured into the V_2CT_x suspension under vigorously stirring for 18 h. Finally, after centrifugation, cleaning with DI water, and freeze-drying overnight, the sediment of RuO_x/ V_2CT_x was achieved.

To synthesize the Ru–Ru₂P/ V_2CT_x product, the RuO_x/ V_2CT_x powder, and sodium hypophosphite monohydrate (NaH₂PO₂·H₂O) were placed in a thermal chemical vapor deposition (CVD) system on a quartz boat, and the sodium hypophosphite monohydrate was kept 5 cm away from the RuO_x/ V_2CT_x powder located at upstream Ar gas flow. The weight ratio of RuO_x/ V_2CT_x powder and NaH₂PO₂·H₂O was chosen as 1:10. The target temperature was fixed at 300 °C for 3 h with ramping rate of 2 °C·min^{−1}, followed by naturally cooling to room temperature.

2.4. Characterizations

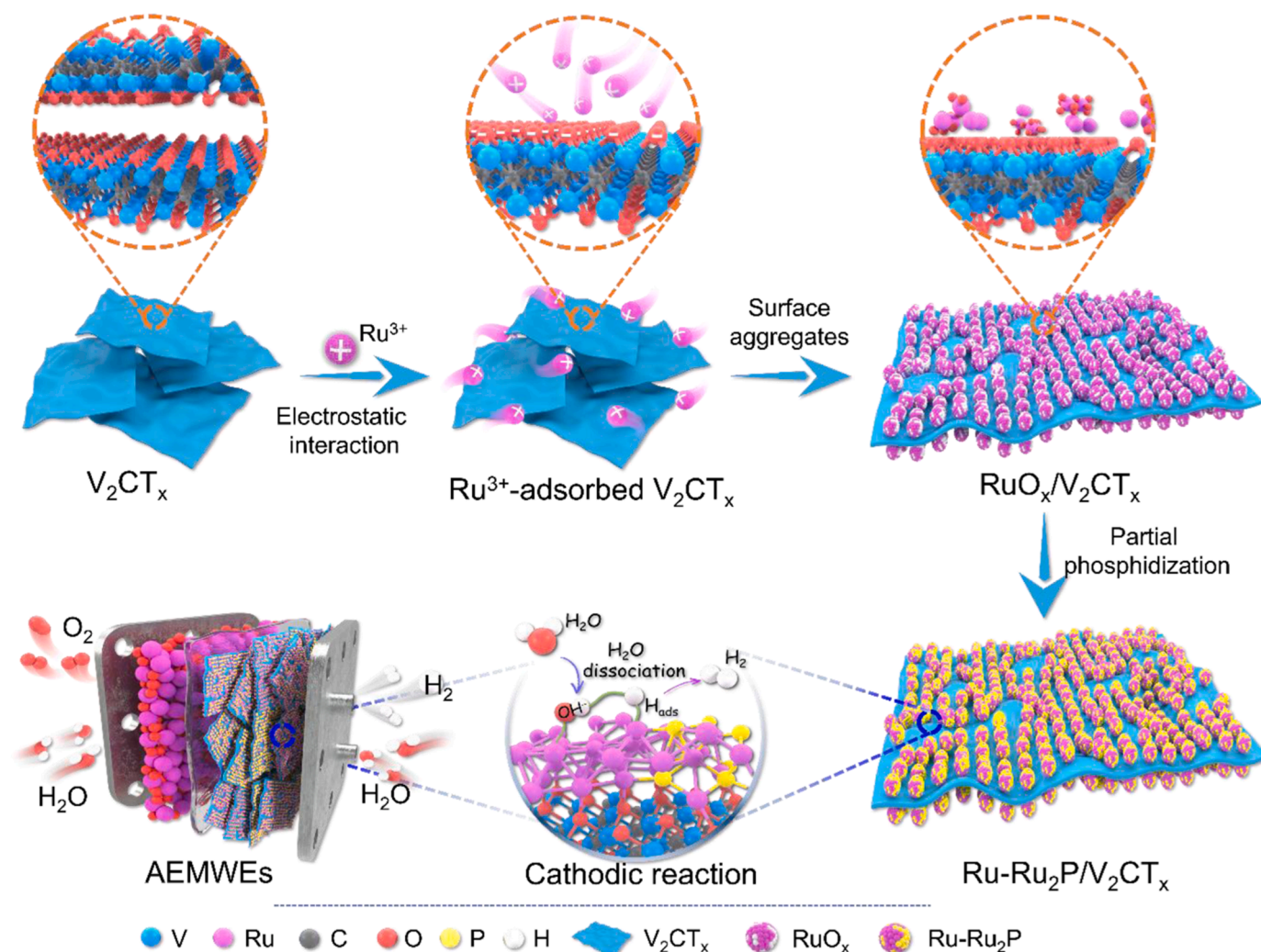
Field emission scanning electron microscopy (SEM) and high-resolution transmission electron microscopy (HR–TEM) were used to probe the morphology of the as-prepared samples on a Supra 40 VP system (Zeiss Co., Germany), and on a JEM–ARM200F system (JEOL, Japan), respectively. The crystallinity of samples was studied by a D/Max 2500 V/PC system (Japan) in the 2θ range 3 – 80° at a scan rate of 2°·min^{−1}. For X-ray photoelectron spectroscopic (XPS) analysis, a Theta Probe (Thermo Fisher Scientific Inc., USA) was employed to investigate the element composition and valence state of different samples. The Raman spectra and zeta-potential of samples were recorded by the micro-Raman spectrum analysis system (RAMANTouchlaser excitation λ = 532 nm; Nanophoton, Japan) and Particle size & Zeta-potential Analyzer NanoPlus (Micromeritics, USA), respectively. The specific surface area was measured using an ASAP 2020 Plus system (Micromeritics Instrument Co., USA). X-ray absorption (XAS) spectra were conducted at room temperature using QuantumLeap-H2000 (Sigray Inc., USA).

3. Results and discussion

3.1. Structure characteristics

Scheme 1 illustrates the synthesis process of the Ru–Ru₂P/ V_2CT_x catalyst by a wet-chemistry approach. First, V_2CT_x nanosheets were synthesized by the HF-etching route, followed by intercalation and delamination. The V_2CT_x MXene colloid is stable in water due to its negatively charged nature caused by abundant surface functional groups (**Fig. S1a**). When positively charged Ru³⁺ precursors were added into the V_2CT_x solution, the black flocculates immediately formed (**Fig. S1b**), proving strong metal-support binding between V_2CT_x and Ru³⁺ through electrostatic attraction to reduce Ru³⁺ to Ru⁶⁺ under the form of RuO_x clusters. This interaction could also effectively prevent the agglomeration of the clusters to ensure the homogenous RuO_x dispersing over the surface of the V_2CT_x nanosheets [17]. Finally, the Ru–Ru₂P/ V_2CT_x catalyst was obtained through partial phosphidization at 300 °C for 3 h. Under the reaction conditions, NaH₂PO₂·H₂O are decomposed into reactive PH₃ and H₂ gases [31,32]. PH₃ can extract the lattice oxygen from RuO_x to form Ru–P species, leading to the phosphidization of RuO_x. Meanwhile, H₂ could reduce RuO_x clusters to enrich metallic Ru phase.

Morphological analysis of the as-prepared V_2CT_x nanosheets derived from field-emission scanning electron microscopy (FE–SEM) (**Fig. S2**) and transmission electron microscopy–energy-dispersive X – ray spectroscopy (TEM–EDX) (**Fig. S3**) confirms the exfoliated state of the few-layer V_2CT_x nanosheets. Following the MXene exfoliation, the surface deposition step enables the in situ nucleation and uniform crystal growth of RuO_x clusters caused by the existence of hydrophilic O-



Scheme 1. Schematic of the preparation pathway for the Ru–Ru₂P/V₂CT_x catalyst via self-electrostatic attraction and phosphidization, and its application in AEMWE.

terminated groups with negatively charged states on the V₂CT_x surface, which effectively act as surfactants, as well as reducing agents, to adsorb positively charged Ru³⁺ ions through electrostatic interactions, and then oxidize them into RuO_x [17]. The RuO_x clusters are homogeneously dispersed on the MXene surface without self-aggregation (Fig. S4 and Fig. S5). The strong chemical interactions between such active RuO_x clusters with functional groups of MXene or their prospective van der Waals forces are well confirmed since they effectively avoid the self-growth and spontaneous agglomeration of RuO_x during a phosphidization procedure at an intermediate temperature of 300 °C to result in monodispersed Ru–Ru₂P clusters on the exfoliated V₂CT_x nanosheets (Fig. 1a and Fig. S6). The atomic force microscope (AFM) analysis of the Ru–Ru₂P/V₂CT_x further points to its thin 2D features of approximately 3.4 nm with a significant enhancement of thickness as well as roughness, as compared to the original V₂CT_x structure (3.1 nm), due to the incorporation of rich Ru–Ru₂P clusters on the MXene surface (Fig. S7). The high-angle annular dark-field scanning transmission electron microscopy (HAADF–STEM) and HR–TEM images of the Ru–Ru₂P/V₂CT_x (Fig. 1b and c) feature the high density of ultrasmall Ru–Ru₂P nanoclusters at a size distribution of 1.87 ± 0.4 nm uniformly attached over the V₂CT_x structure. The STEM image and SAED spectrum of those clusters reveal their high-quality crystallinity (Fig. 1d), along with the presence of specific lattice fringes at area A1 and A2, which are consistent with the interspacing of 0.21 and 0.24 nm derived from the

(101) crystal plane of a Ru metal phase (Fig. 1e) and the (112) crystal planes of Ru₂P phase (Fig. 1f), respectively.

Furthermore, the EDS mapping images in Fig. 1g also indicate the homogeneous distribution of V, Ru, C, O, and P elements over a surveyed area of the material structure, confirming the successful preparation of Ru–Ru₂P nanoclusters anchored on V₂CT_x. Such resulting structural characteristics of the Ru–Ru₂P/V₂CT_x hybrid may exhibit a strong electronic coupling that boosts both electron and ion transfer across the interface, which is highly favorable for accelerating the kinetics of catalytic reactions. The X-ray diffraction (XRD) was applied to evaluate the crystalline properties of the synthesized Ru–Ru₂P/V₂CT_x and V₂CT_x materials. Fig. 1h shows a visible peak at 2θ of 4.5° consistent with an interlayer spacing of ≈ 1.96 nm caused by the characteristic of the (002) crystal plane from V₂CT_x [29]. As compared to XRD pattern of V₂AlC MAX (Fig. S8), the shift of the (002) peak, from 13.39° in V₂AlC MAX to 4.5° for V₂CT_x, is attributed to the successful removal of Al from V₂AlC and subsequent expansion of the d(002)-spacing from 0.66 nm to 1.96 nm, respectively [33,34]. The presence of some small peaks could be attributed to the incomplete etching state in the final MXene product, as similarly observed in previous publications [35]. After coupling with Ru–Ru₂P hetero-clusters, the Ru–Ru₂P/V₂CT_x hybrid exhibits a specific diffraction peak located at 2θ of 42.4°, which could be referred to the (101) crystal plane of metallic hexagonal Ru phase (JCPDS no. 88–1734), along with the presence of some small peaks at 2θ of 29.7°,

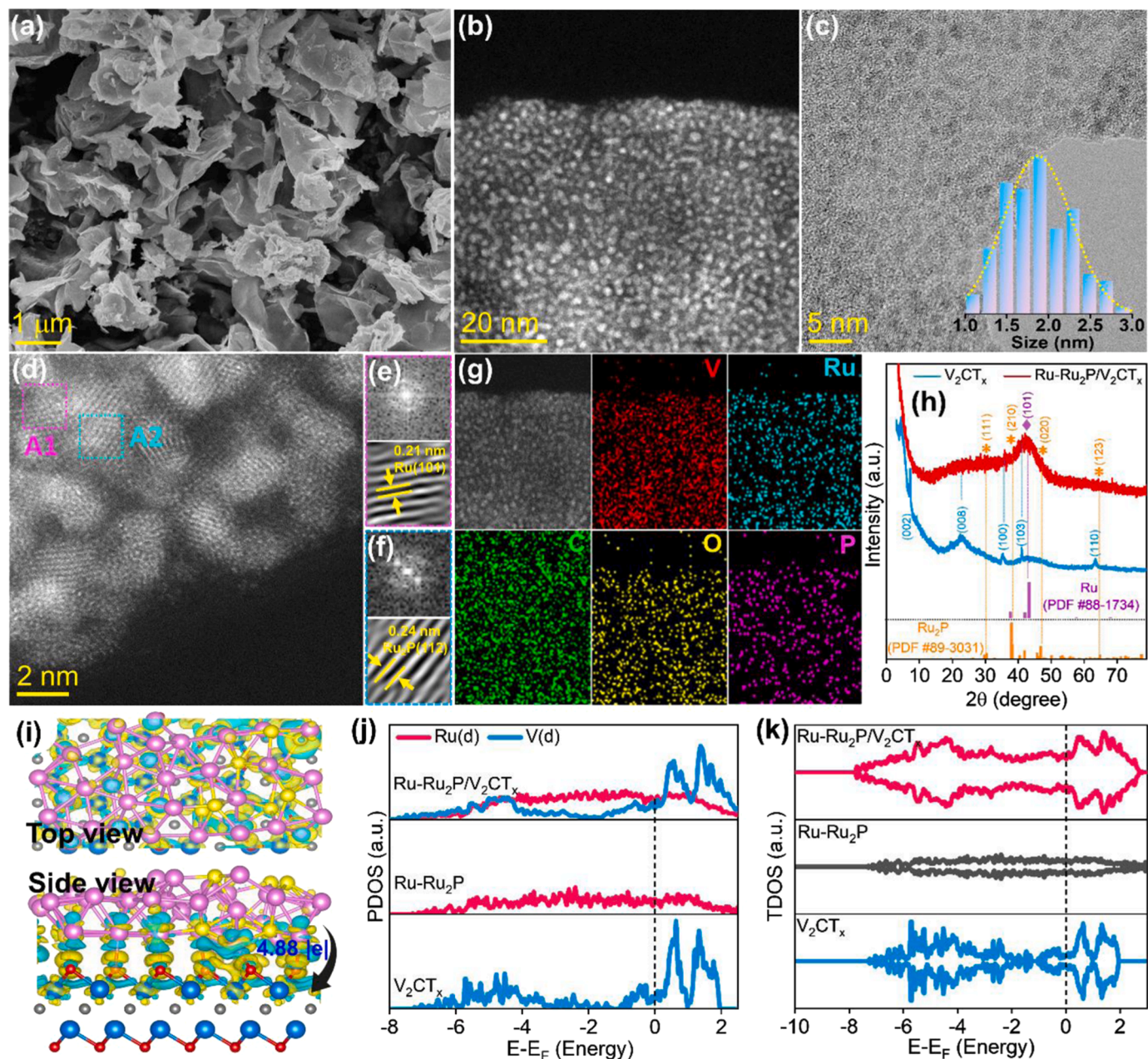


Fig. 1. (a) SEM and (b) STEM images of Ru–Ru₂P/V₂CT_x. (c) TEM image of Ru–Ru₂P/V₂CT_x (Inset: size histogram of Ru–Ru₂P nanoclusters). (d) HAADF–STEM image of Ru–Ru₂P/V₂CT_x and marked area of Ru and Ru₂P crystalline phase illustrated by A1 and A2 dashed rectangular. Fast Fourier transform and inverse fast Fourier transform patterns of (e) Ru and (f) Ru₂P phases. (g) Corresponding EDX mapping of the Ru–Ru₂P/V₂CT_x. (h) XRD patterns of Ru–Ru₂P/V₂CT_x and V₂CT_x. (i) Charge density differences of Ru–Ru₂P/V₂CT_x models are illustrated by top- and side-views, whereas the cyan and yellow color indicate the accumulation and depletion of electrons, respectively. (j) The projected DOS of Ru(d) and V(d) orbitals, and (k) the total DOS plots of the Ru–Ru₂P/V₂CT_x, Ru–Ru₂P, and V₂CT_x models.

38.6°, 47.2°, and 64.3° relating to the (111), (210), (020), and (123) crystal planes, respectively, of orthorhombic Ru₂P phase (JCPDS no. 89–3031). Notably, the low intensity and weak diffraction peak of Ru₂P might be explained by the incomplete phase transition at 300 °C, further evidencing the co-existence of two components [31,36]. In contrast, XRD pattern of RuO_x/V₂CT_x sample (Fig. S9) exhibits a board diffraction peak located at 2θ of 28°, assigning to the RuO₂ phase (JCPDS no. 40–1290). Interestingly, the XRD pattern of the hybrid material also indicates the disappearance of the (002) peak in the surveyed 2θ range, caused by its significant downshift to small angle lower than 4.5°, attributed to the further expansion of interlayer spacing between layers caused by the intercalation/deposition of numerous Ru–Ru₂P clusters

[16,37,38]. This implies that the anchored Ru–Ru₂P clusters can effectively expand the interlayer spacing between V₂CT_x layers, which is thus expected to accelerate the electrolyte ions diffusion/transport during the catalytic process [17]. Raman analysis of the V₂CT_x shows some broad peaks centered at 100–600 and 933 cm^{−1}, which result from the in-plane/out-of-plane vibrations of V atoms and the vibration of functional surface groups (Fig. S10) [39]. The typical carbon fingerprint signals found in the region from 1200 to 1800 cm^{−1} indicate the formation of amorphous carbon due to the over-etching of the V₂AlC [40]. In the case of the Ru–Ru₂P/V₂CT_x, the abovementioned peaks of the V₂CT_x are apparently shifted and attenuated due to the correlated structural disorder after coupling with the Ru–Ru₂P clusters. In addition,

the carbon fingerprint peaks are not detectable because the V_2CT_x surface was fully covered by the Ru–Ru₂P nanoclusters, hence the degree of graphitization was hard to expose [41]. The electronic structure changes in the Ru–Ru₂P/ V_2CT_x were revealed by density functional theory (DFT) calculations with an early reported hypothesis of strong metal-support interaction between Ru–Ru₂P and V_2CT_x via Ru–O–V bonds. Fig. 1i shows a unique electronic structure with charge density difference at the interface of the hybrid structure caused by the significant electron redistribution, which indicates that 4.88 |e| is transferred from the Ru–Ru₂P to V_2CT_x . As can be seen in Fig. 1j, the projected density of states (PDOS) of V(d) in the region [0,2] are redistributed to higher energy levels in Ru–Ru₂P/ V_2CT_x in comparison with that of V_2CT_x . Additionally, the 2nd PDOS peak in Ru–Ru₂P/ V_2CT_x (at the higher energy) became higher than the 1st peak (near the Fermi level), allowing that energy region is broadened to higher energy. This change can be

expected to result in an enhancement in mobility of V(d) electrons in Ru–Ru₂P/ V_2CT_x sample. In addition, total DOS of the Ru–Ru₂P/ V_2CT_x exhibits a higher value at the Fermi level (E_F) than individual Ru–Ru₂P or V_2CT_x (Fig. 1k), proving high electronic conductivity and fast electron transfer capability [42]. These theoretical results further confirm the exciting electronic structure of the Ru–Ru₂P/ V_2CT_x with an optimized charge reconfiguration and strong metal-support interactions, which may lead to the well-adjusted bonding between reactant intermediates and catalyst [43,44], as well as the promoted charge transfer during the electrochemical reaction.

The X-ray absorption (XAS) and X-ray photoelectron spectroscopy (XPS) were used to examine the chemical state and surface electronic structure of the synthesized catalysts. Fig. 2a shows chemical state and local structure of Ru in Ru–Ru₂P/ V_2CT_x , Ru metal, and RuO₂ materials through the X-ray absorption near edge structure (XANES) spectra,

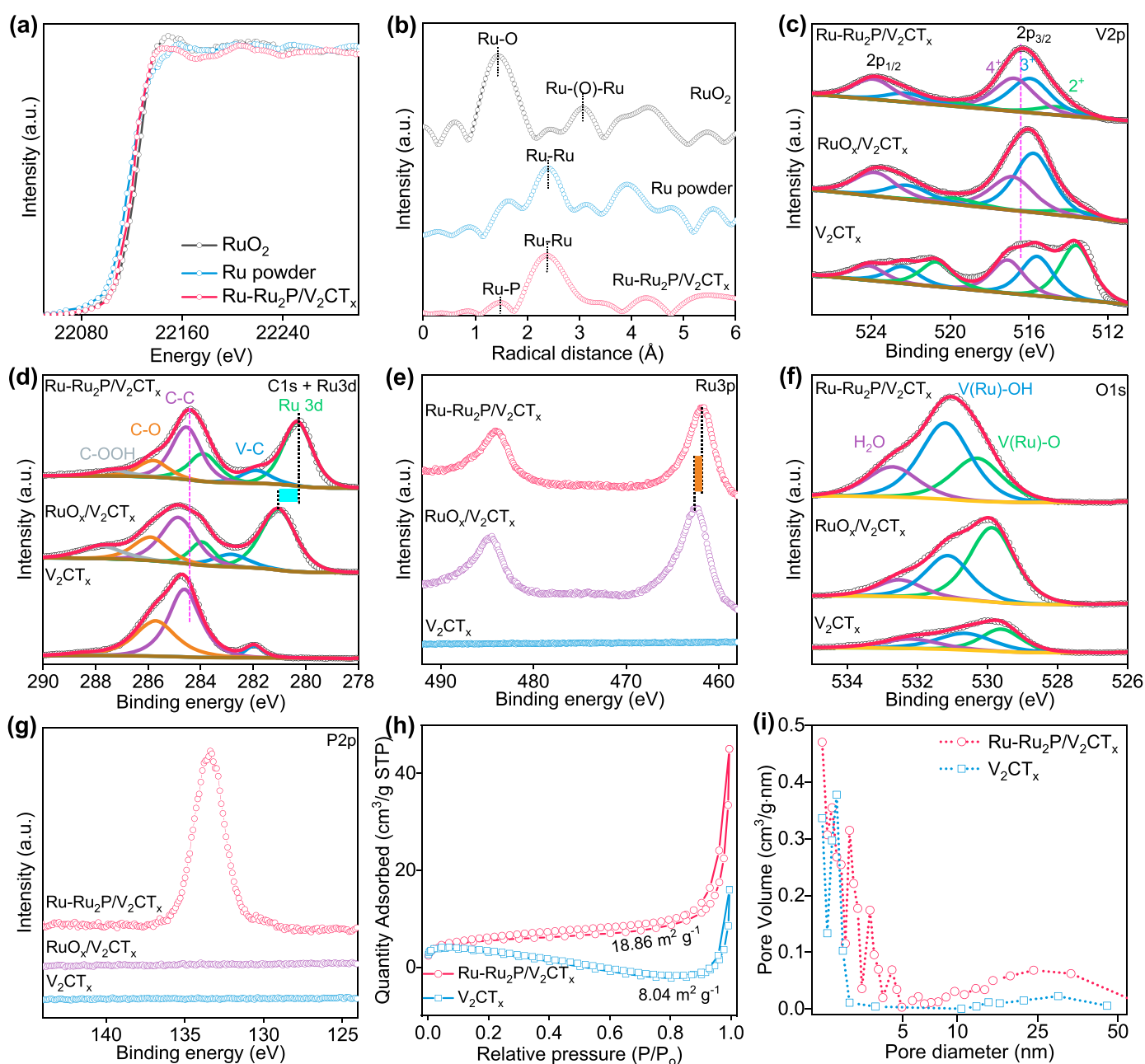


Fig. 2. (a) XANES and (b) FT-EXAFS spectra for Ru K-edge of Ru–Ru₂P/ V_2CT_x , Ru metal, and RuO₂. High-resolution XPS spectra of the (c) V2p, (d) C1s + Ru3d, (e) Ru3p, (f) O1s, and (g) P2p for the Ru–Ru₂P/ V_2CT_x , RuO_x/ V_2CT_x , and V_2CT_x . (h) N₂ adsorption/desorption isotherms and (i) pore size distribution of the Ru–Ru₂P/ V_2CT_x and V_2CT_x . Note that the graph was plotted by the y-axis value times 100.

which indicate the location of absorption edge position from Ru K-edge of Ru–Ru₂P/V₂CT_x is between that of Ru metal and RuO₂, suggesting the phase transformation from RuO_x clusters to Ru–P pieces upon phosphidization [31]. In addition, the corresponding Fourier transform extended X-ray absorption fine structure (FT-EXAFS) spectrum of the Ru–Ru₂P/V₂CT_x shows only specific peaks at ~ 1.9 and ~ 2.4 Å, corresponding to Ru–P and Ru–Ru bonding, respectively (Fig. 2b), further confirming the formation of new electronic states of Ru in Ru–Ru₂P structure caused by the conversion of RuO_x to Ru–Ru₂P structure [36, 45]. The XPS survey spectra in Fig. S11 shows the existence of V, C, Ru, O, and P elements, consistent with the STEM–EDX result. The high-resolution V2p spectrum of the Ru–Ru₂P/V₂CT_x indicates three pairs of peaks centered at 523.8/516.7, 522.0/515.9, and 519.8/514.5 eV, corresponding to the V2p_{1/2}/2p_{3/2} orbitals of V⁴⁺, V³⁺, and V²⁺, respectively (Fig. 2c) [35]. Interestingly, the V2p signal of the Ru–Ru₂P/V₂CT_x reveals the predominant intensities of V⁴⁺ and V³⁺ portions, while there is a significant reduction of V²⁺ portion, as compared to those of the V₂CT_x. This alternation indicates the electronic change due to the incorporation with Ru–Ru₂P clusters into the V₂CT_x backbone. Fig. 2d shows the high-resolution (C1s + Ru3d) XPS spectra

of the Ru–Ru₂P/V₂CT_x, RuO_x/V₂CT_x, and V₂CT_x. Four peaks at binding energies of 287.3, 285.8, 284.5, and 281.8 eV are consistent with the features of C–OOH, C–O, C–C, and C–V bonding, respectively [46]. In addition, two peaks located at binding energies of 283.8 and 280.2 eV are indexed to Ru 3d_{1/2} and 3d_{3/2}, respectively [47]. Fig. 2e shows the high-resolution Ru3p XPS spectra of the materials with two peaks of the Ru3p_{1/2} and 3p_{3/2} at binding energies of 484.0 and 461.8 eV, respectively [48]. Impressively, it is discovered that while the V2p peak of the Ru–Ru₂P/V₂CT_x is shifted to high binding energy, its Ru3d and Ru3p peaks are moved to lower binding energy values, as compared to the pure V₂CT_x or RuO_x/V₂CT_x. Such phenomena involve the O replacement by P during the phosphidization process or charge transfer between active clusters and the MXene surface, which lead to the charge redistribution with specific valence states of components in the Ru–Ru₂P and V₂CT_x [47,49], which is highly beneficial to improve the catalytic activity and durability [31,47]. Fig. 2f shows the high-resolution O1s XPS spectra, which were deconvoluted into three characteristic peaks located at binding energies of 532.7, 531.2, and 530.5 eV, relating to the adsorbed water, V(Ru)–OH bonding, and V(Ru)–O bonding, respectively [33]. Fig. 2g shows the high-resolution P2p XPS spectrum of the

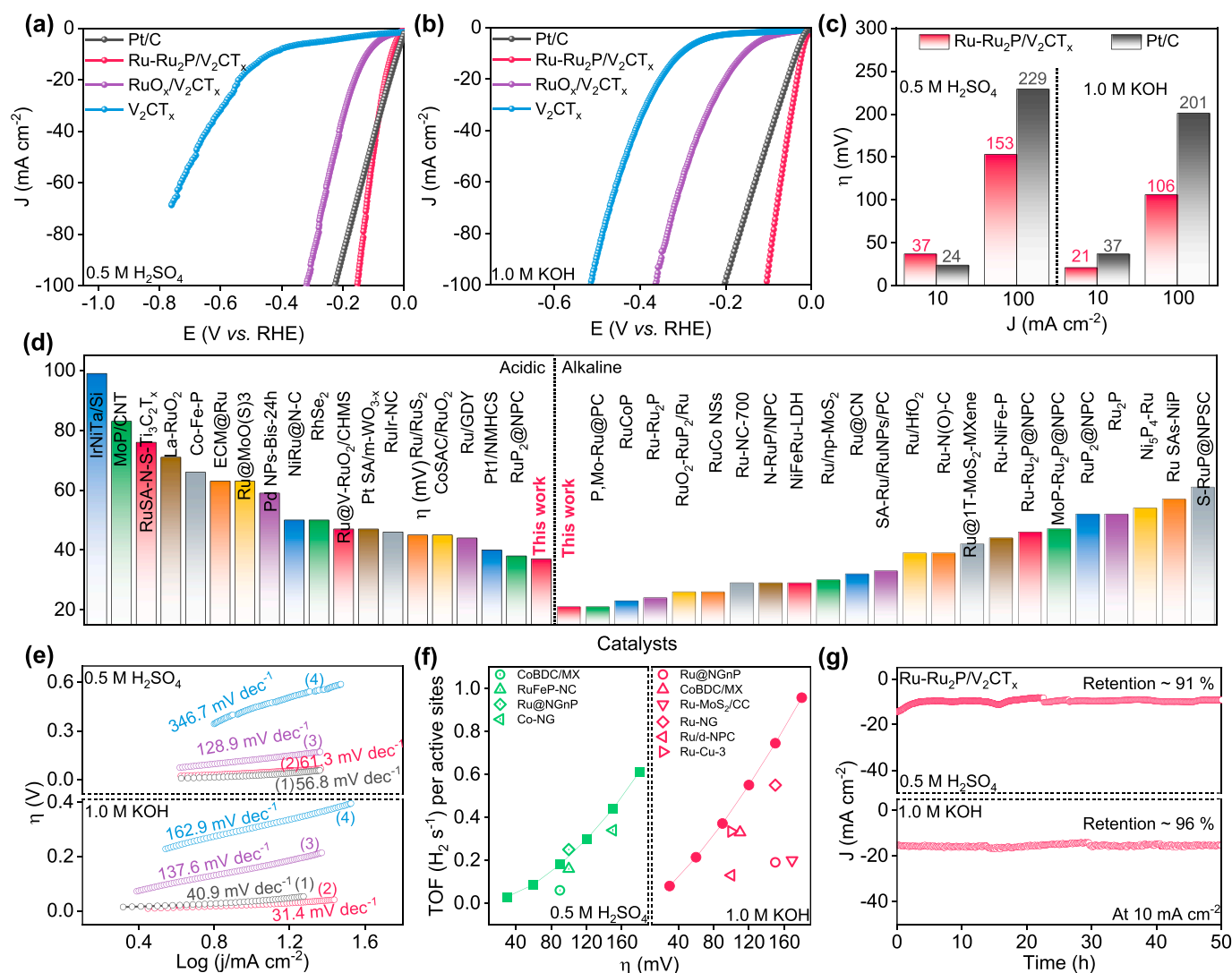


Fig. 3. HER performances of the prepared catalysts in electrolyte media: LSV curves of catalysts with a scanning rate of 5 mV·s⁻¹ in (a) 0.5 M H₂SO₄, and (b) 1.0 M KOH. (c) Comparison of η_{HER} at 10 and 100 mA·cm⁻² between commercial Pt/C and Ru–Ru₂P/V₂CT_x. (d) Comparison of the HER performance at η_{10} between Ru–Ru₂P/V₂CT_x and various published electrocatalysts. (e) The corresponding Tafel plots of (1) commercial Pt/C, (2) Ru–Ru₂P/V₂CT_x, (3) RuO_x/V₂CT_x, and (4) V₂CT_x in electrolyte media. (f) TOF values of the Ru–Ru₂P/V₂CT_x and recent reported electrocatalysts in electrolyte media. (g) Stability tests of the Ru–Ru₂P/V₂CT_x operated at 10 mA·cm⁻² over 50 h in acidic and alkaline environments.

Ru–Ru₂P/V₂CT_x with a strong peak centered at a binding energy of 133.4 eV, derived from the P in Ru₂P structure [47]. The specific surface area of the Ru–Ru₂P/V₂CT_x and V₂CT_x materials was measured by the technique of N₂ adsorption–desorption isotherms at 77 K (Fig. 2h). The Ru–Ru₂P/V₂CT_x sample exhibits a large specific surface area of 18.86 m²·g^{−1}, which is 2.34 times higher than that of the pure V₂CT_x (8.04 m²·g^{−1}), even after the MXene surfaces are attached with abundant Ru–Ru₂P clusters with as high as 24.3 wt% of Ru, analyzed by inductively coupled plasma-optical emission spectroscopy (ICP–OES). Such material also possesses a high pore volume and mesoporous features with pore distribution in the range of 3–10 nm, suggesting that its structure may reveal more exposed active centers to catalyze the reactions (Fig. 2i).

3.2. Catalytic performances

The HER performance of the synthesized catalysts was studied using a three-electrode configuration in 0.5 M H₂SO₄ and 1.0 M KOH environments in Fig. 3a and b, which show the superior catalytic activity of the Ru–Ru₂P/V₂CT_x, as compared to the RuO_x/V₂CT_x and V₂CT_x materials. Specifically, Fig. 3c exhibits that the Ru–Ru₂P/V₂CT_x needs low overpotential of 37 and 21 mV to reach a current density of 10 mA·cm^{−2} in 0.5 M H₂SO₄ and 1.0 M KOH, respectively, which is much smaller than that of the RuO_x/V₂CT_x of 121 and 158 mV, and of the V₂CT_x of 421 and 301 mV. In addition, its HER behaviors are also comparable with a reference catalyst sample derived from the commercial Pt/C (with 20 wt % of Pt loaded onto graphitized carbon), which requires low overpotential of 24 mV in acid and 37 mV in alkaline to achieve a current density of 10 mA·cm^{−2}. The Ru–Ru₂P/V₂CT_x is further demonstrated to be one of the extraordinary HER electrocatalysts since it is compared with recently reported MXene-based/Ru-based HER candidates working in both acidic and alkaline environments at 10 mA·cm^{−2} (Fig. 3d, and Tables S1 and S2). In another regard, the HER kinetics of the catalysts were investigated in Fig. 3e, which exhibits the small Tafel slope of 61.3 and 31.4 mV·dec^{−1} for the Ru–Ru₂P/V₂CT_x in 0.5 M H₂SO₄ and 1.0 M KOH, respectively, which are almost similar to those of the Pt/C of 56.8 and 40.9 mV·dec^{−1}, but much smaller than those of the RuO_x/V₂CT_x of 128.9 and 137.6 mV·dec^{−1} and of the V₂CT_x of 346.7 and 162.9 mV·dec^{−1}, respectively. The small Tafel slope values of the Ru–Ru₂P/V₂CT_x, as compared to the individual material in alkaline and acid, implies its fast HER kinetics caused by the synergistic effect of the Ru–Ru₂P and V₂CT_x component. In addition, the achieved Tafel results inform that the HER kinetic of the Ru–Ru₂P/V₂CT_x follows the Volmer–Tafel mechanism in alkaline medium [50], while its HER kinetic occurs by the Volmer–Heyrovsky mechanism in acidic medium [51], in which Tafel and Heyrovsky are the rate-determination steps, respectively [52]. The exchange current density (*j*₀) of catalysts can be obtained by extrapolating the Tafel plots. The Ru–Ru₂P/V₂CT_x sample shows a high *j*₀ value of 2.08 mA·cm^{−2}, which is 1.73 and 2.70 times higher than those of the RuO_x/V₂CT_x (1.20 mA·cm^{−2}) and V₂CT_x (0.7 mA·cm^{−2}), respectively, in 0.5 M H₂SO₄ (Fig. S12). Meanwhile, in 1.0 M KOH medium, the Ru–Ru₂P/V₂CT_x material also presents a high *j*₀ value of 1.58 mA·cm^{−2}, much better than their counterparts (Fig. S13). The charge–transfer properties of different materials were systematically inspected by electrochemical impedance spectroscopy (EIS). In both acidic and alkaline media, the Ru–Ru₂P/V₂CT_x offers the smallest semicircle, as compared to the RuO_x/V₂CT_x and V₂CT_x (Fig. S14), suggesting the super charge transfer of its structure, resulting from the combination between Ru–Ru₂P and V₂CT_x. Moreover, *operando* EIS measurement was also employed at different potentials to understand the elementary reactions during the HER process in alkaline media. As expected, only one phase angle appears for the Pt/C and Ru–Ru₂P/V₂CT_x within the frequency range 10⁵ to 10^{−2} Hz, demonstrating that the HER process followed the Volmer–Tafel mechanisms (Fig. S15) [53], which is well consistent with the low Tafel slope of the Ru–Ru₂P/V₂CT_x and commercial Pt/C in alkaline media. The *operando*

Raman spectroscopy was performed to further disclose the HER mechanism in 1.0 M KOH (Fig. S16). As displayed in Fig. S17a, the Raman spectrum of the Ru–Ru₂P/V₂CT_x exhibits a broad peak located around 3500 cm^{−1}, corresponding to interfacial water molecule vibration. Furthermore, this peak could be deconvoluted into three components centered at 3225, 3450, and 3615 cm^{−1} for v1, v2, and v3, respectively (Fig. S17b). The first two peaks (v1 and v2) are assigned to tetrahedrally coordinated water and trigonally coordinated water, respectively. This coordinated water directly participates in the HER process [54], while the third peak (v3) is assigned to the dangling O–H bond of the interfacial water that is considered as inactive water [55]. Fig. S17c indicates that the proportion of v3 linearly decreases with a negative shift of the applied potential, proving that the water dissociation on the surface of Ru–Ru₂P/V₂CT_x catalyst was accelerated [56]. To further identify the origin of the outstanding HER activities for different materials, Figs. S18 and S19 show the calculated turnover frequency (TOF) results. The TOF value of the Ru–Ru₂P/V₂CT_x is found to be 0.23 and 0.43 s^{−1} in 0.5 M H₂SO₄ and 1.0 M KOH, respectively, at η = 0.1 V, much higher than that of RuO_x/V₂CT_x (0.04 and 0.02 s^{−1}), V₂CT_x (0.01 and 0.009 s^{−1}), commercial Pt/C (0.15 and 0.16 s^{−1}) in 0.5 M H₂SO₄ and 1.0 M KOH, respectively; and even beyond the recently reported MXene/Ru-based HER electrocatalysts (Fig. 3f and Table S3). This result confirms the high intrinsic activities of the Ru–Ru₂P/V₂CT_x that result in remarkable electrocatalytic HER performance. In another regard, the electrochemical double-layer capacitance (*C*_{dl}) of the materials was evaluated to estimate their electrochemically active surface area (ECSA). In 0.5 M H₂SO₄, the Ru–Ru₂P/V₂CT_x possesses a high *C*_{dl} value of 18.5 mF cm^{−2}, almost 1.62 and 2.56 times higher than that of the RuO_x/V₂CT_x (11.4 mF cm^{−2}) and V₂CT_x (7.2 mF cm^{−2}), respectively (Fig. S20). The Ru–Ru₂P/V₂CT_x also exhibits the best *C*_{dl} value of 46.4 mF cm^{−2} among all the synthesized materials in 1.0 M KOH (Fig. S21). Fig. S22 shows the ECSA-normalized LSV response with the specific activity order of Ru–Ru₂P/V₂CT_x > RuO_x/V₂CT_x > V₂CT_x. A similar trend is also observed for the mass-normalized LSV responses of the catalysts in 0.5 M H₂SO₄ and 1.0 M KOH (Fig. S23), demonstrating the enhanced intrinsic specific activity and mass activity of the Ru–Ru₂P/V₂CT_x toward HER in both the acidic and alkaline environments. The durability of the Ru–Ru₂P/V₂CT_x and Pt/C materials was investigated by continuous amperometry measurements in acidic and alkaline media. The HER activity of Pt/C exhibits a rapid decline of current response after only 25 h operation (Figs. S24a and S25a), along with a significant increase of overpotential as recorded by LSV measurement (Fig. S24b and S25b) caused by the phenomena of Pt NPs aggregation/dissolution and carbon corrosion [57]. Meanwhile, the Ru–Ru₂P/V₂CT_x catalyst displays well-retained activity with almost 91 % and 95 % retention of the initial current over 50 h operation in acidic and alkaline medium, respectively (Fig. 3g).

The HER LSV responses of the Ru–Ru₂P/V₂CT_x at initial and after long-term stability test overlap well in both the 0.5 M H₂SO₄ and 1.0 M KOH (Fig. S26). In addition, morphological analysis of the post-HER Ru–Ru₂P/V₂CT_x catalyst still displays thin-sheet characters with well-maintained content of respective elements (Figs. S27 and S28), indicating the robust structure of Ru–Ru₂P/V₂CT_x after stability tests. Furthermore, the XPS spectra of the post-HER Ru–Ru₂P/V₂CT_x also evidence no visible change of chemical valance state for active components at the surface (Figs. S29 and S30), demonstrating the outstanding electrocatalytic activity and durability for long-term HER operation under harsh media. To reveal the prospective HER performance of the Ru–Ru₂P/V₂CT_x catalyst in pH-universal environment, its catalytic behavior was also examined in a neutral medium of 1.0 M PBS electrolyte (Fig. S31a). The Ru–Ru₂P/V₂CT_x catalyst can also be observed to achieve current densities of 10 and 50 mA·cm^{−2} at low overpotentials of 95 and 296 mV, respectively, which are significantly better than those of RuO_x/V₂CT_x (318 and 645 mV), V₂CT_x (437 and 816 mV), and even relatively comparable to those of the Pt/C (53 and 238 mV), revealing it as the most efficient HER electrocatalyst working in pH-neutral

conditions (Fig. S31b and Table S4). In addition, the small Tafel slope values of 93.5 and 135.6 mV·dec⁻¹ observed in Fig. S31c for the Pt/C and Ru–Ru₂P/V₂CT_x, respectively, imply their fast HER kinetics via the Volmer–Heyrovsky mechanism in 1.0 M PBS solution. This is well supported by the analyses of EIS, exchange current density, and ECSA in Figs. S32, S33, and S34, respectively, which indicate the lower charge transfer resistance, higher exchange current response, as well as the larger ECSA value of the Ru–Ru₂P/V₂CT_x among the other synthesized catalysts. In addition, durability test of the Ru–Ru₂P/V₂CT_x in Fig. S31d also confirms a good current retention of 93 % after an operation period of 50 h. The intrinsic HER properties of the catalysts in 1.0 M PBS solution were also investigated with ECSA-normalized specific activity, mass activity, and TOF values in Figs. (S35 and S36a), Figs. S36b, and Figs. S36c, respectively. The achieved results indicate that the Ru–Ru₂P/V₂CT_x catalyst possesses the best specific activity, mass activity, and TOF compared to the counterparts, further validating its excellent intrinsic catalytic properties toward HER in neutral electrolyte solution, as well as in a wide-range pH environment.

To understand the role of specific interfaces derived from the combination of Ru–Ru₂P and V₂CT_x for the improved HER performance in the pH-universal environment, theoretical study was conducted for the three structures of the Ru–Ru₂P/V₂CT_x, Ru–Ru₂P, and V₂CT_x in Fig. 4a,

and Fig. S37. The electronic structure of materials was observed by the PDOS of Ru 3d orbital, which exhibits higher state of the Ru–Ru₂P/V₂CT_x at the E_F, compared to the pure Ru–Ru₂P (Fig. 4b), implying that the good hybridization between Ru–Ru₂P and V₂CT_x leads to the favorable charge configuration for active Ru-based centers. According to the d-band center theory, the adsorbate valence states could electronically interact with the *d* states of a metal surface, forming bonding and antibonding states. Since the antibonding state is above the E_F, it could promote the adsorption of hydrogen intermediates during HER, and vice versa [58]. In this context, the d-band centers of the Ru–Ru₂P/V₂CT_x and Ru–Ru₂P were –1.76 and –1.80 eV, respectively, suggesting the upshift of the d-band center of Ru–Ru₂P/V₂CT_x to increase antibonding states above the E_F, thus enhancing the interaction with the adsorbed molecule [59]. In addition, the d-band shift of Ru–Ru₂P/V₂CT_x to the E_F is also expected to weaken the binding strength of H* adsorption and enable easy desorption [60]. Fig. S38 shows the average potential distribution along the Z-direction of the Ru–Ru₂P/V₂CT_x structure, which confirms the electron flow from Ru–Ru₂P to V₂CT_x, consistent with the charge density difference results. It is also well-known that the Gibbs free energy of hydrogen ($|\Delta G_{H^*}|$) of an HER electrocatalyst close to zero is ideal for optimum hydrogen binding strength [61].

Fig. 4c shows the calculated ΔG_{H^*} of –0.15 eV on the Ru–Ru₂P/

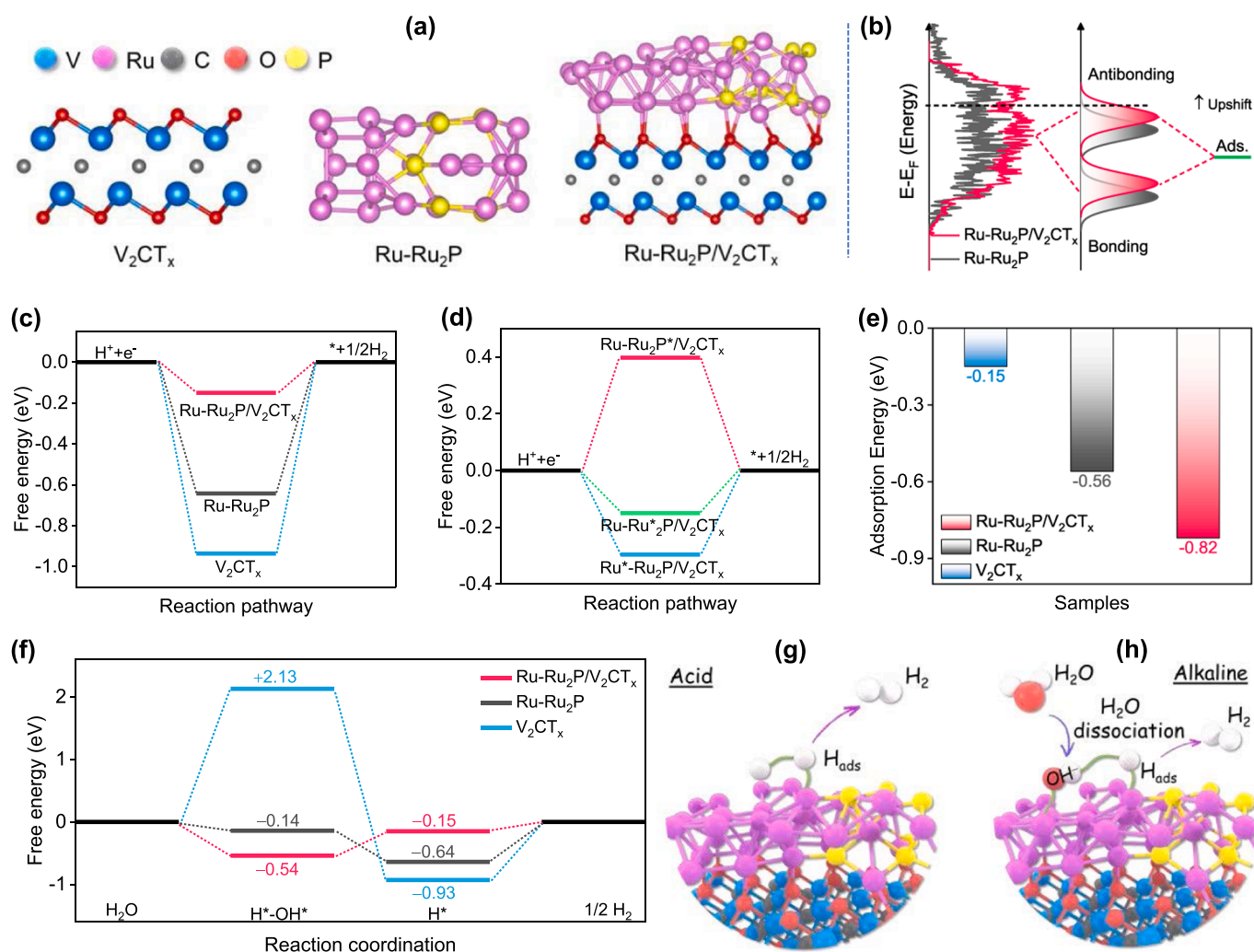


Fig. 4. Understanding the HER mechanism of the Ru–Ru₂P/V₂CT_x and counterparts via the DFT approach: (a) Atomic models of the Ru–Ru₂P/V₂CT_x, Ru–Ru₂P, and V₂CT_x structures. (b) PDOS of Ru 3d orbitals derived from the Ru–Ru₂P/V₂CT_x and Ru–Ru₂P, and the corresponding DOS schematics illustrating the d-band center and bond formation. (c) ΔG_{H^*} of the Ru–Ru₂P/V₂CT_x, Ru–Ru₂P, and V₂CT_x. (d) ΔG_{H^*} values at different active centers in the Ru–Ru₂P/V₂CT_x model. (e) H₂O adsorption energy, and (f) Gibbs free energy diagrams the Ru–Ru₂P/V₂CT_x, Ru–Ru₂P, and V₂CT_x towards HER in alkaline. (g and h) Illustrated HER pathways of the Ru–Ru₂P/V₂CT_x in acid and alkaline.

V_2CT_x in acidic media, which is relatively better than the Pt(111) surface (-0.22 eV, Fig. S39). Meanwhile, the individual Ru–Ru₂P or V_2CT_x exhibit worse hydrogen adsorption behavior with a more negative ΔG_{H^*} value of -0.64 or -0.93 eV, respectively, revealing their unfavorable H^* adsorption due to too strong hydrogen binding strength. To identify the real active sites on the Ru–Ru₂P/ V_2CT_x model towards HER, we have investigated all possible catalytic active centers, including Ru in Ru phase, Ru in Ru₂P phase, and P in Ru₂P phase (Fig. 4d). The results show that the Ru in Ru₂P phase possesses a ΔG_{H^*} value of -0.15 eV, which is better than that of Ru in Ru phase and P in Ru₂P phase with their ΔG_{H^*} values of -0.29 and 0.39 eV, respectively, suggesting that the Ru sites in Ru₂P phase are the primary active sites for catalyzing the HER process.

Considering the HER process in alkaline media, its activity is determined by two crucial factors: the water dissociation (ΔG_{H_2O}), and the $|\Delta$

$G_{H^*}|$ value, in which the water dissociation is generally considered as the rate-determining step on the catalytic surface [24,62]. Fig. 4e shows that the Ru–Ru₂P/ V_2CT_x displays the more negative adsorption energy of H_2O molecules (-0.82 eV) as compared to the Ru–Ru₂P (-0.56 eV) or V_2CT_x (-0.15 eV), suggesting its favorite H_2O activation. To gain insights from a thermodynamic point of view, the Gibbs free energy diagram of alkaline HER was calculated. According to Fig. 4f, the ΔG_{H_2O} on V_2CT_x is a thermodynamic endothermic process with an energy barrier of 2.13 eV, while this process is an exothermic process for Ru–Ru₂P/ V_2CT_x and Ru–Ru₂P with energy barrier of -0.54 and -0.14 eV, respectively, suggesting their HER thermodynamically favorable. Particularly, the more negative free energy in Ru–Ru₂P/ V_2CT_x indicates energetical satisfactory for an easy process of water dissociation [62], thus further accelerating HER kinetics. The schematic of the proposed HER pathways on Ru–Ru₂P/ V_2CT_x in acidic

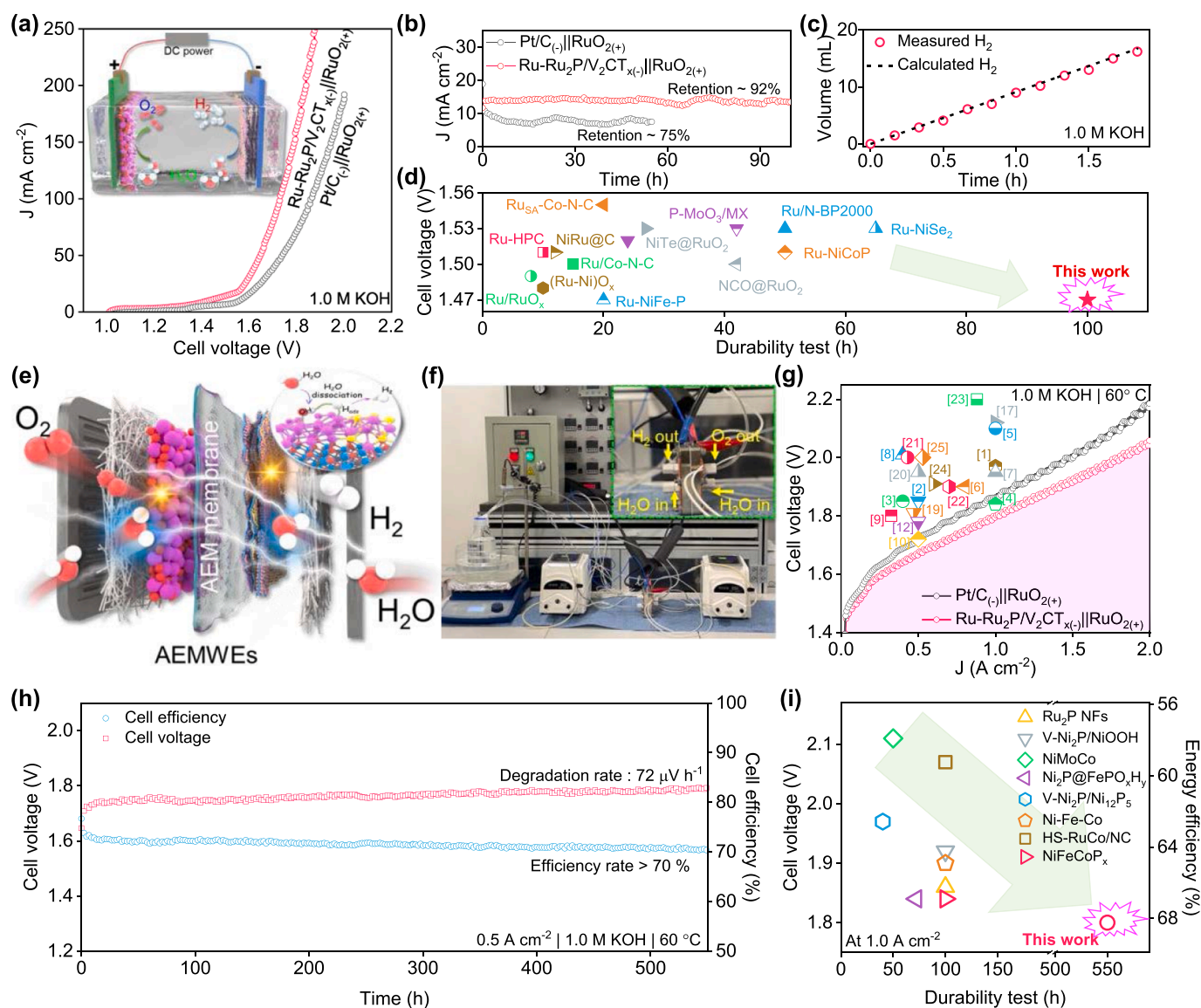


Fig. 5. Performance of two-electrode electrolysis cell and AEMWE stack using the Pt/C or Ru–Ru₂P/ V_2CT_x HER catalyst: (a) LSV curves with a scanning rate of 5 mV s⁻¹ of the Ru–Ru₂P/ V_2CT_x (-)||RuO₂(+) and commercial Pt/C(-)||RuO₂(+) in alkaline (Inset: A schema of the two-electrode electrolysis cell in alkaline). (b) Stability test of the Ru–Ru₂P/ V_2CT_x (-)||RuO₂(+) and Pt/C(-)||RuO₂(+) operated at 10 mA cm⁻² in alkaline. (c) The Faradaic efficiency of Ru–Ru₂P/ V_2CT_x (-)||RuO₂(+) derived from experimental and theoretical amount of H₂ gases as a function of time. (d) Comparison of cell voltage at 10 mA cm⁻² and durability of Ru–Ru₂P/ V_2CT_x (-)||RuO₂(+) with early reported cell systems. (e) Schematic and (f) photograph of the developed AEMWE stack. (g) I – V curves of AEMWE using Pt/C or Ru–Ru₂P/MX as cathodic catalyst and RuO₂ as anodic catalyst at 60 °C in 1.0 M KOH. (h) Chronopotentiometry testing of AEMWE at 0.5 A cm⁻² and 60 °C. (i) Comparison of the cell performance (cell voltage and cell efficiency) at 1.0 A cm⁻² and the operational stability of the developed AEMWE with recently reported systems. (The x-axis presents the operation time; the left and right y-axis represent the cell voltage and efficiency at 1.0 A cm⁻², respectively).

and alkaline media clearly demonstrates that coupling Ru–Ru₂P with V₂CT_x could effectively regulate the d-band center and tune electronic structures, promoting the adsorption and desorption of reaction intermediates, subsequently improving the HER catalytic behavior in various pH conditions (Fig. 4g and h).

Inspired by the superior HER performance of Ru–Ru₂P/V₂CT_x in pH-universal environment, especially in alkaline medium, a two-electrode electrolyzer device was constructed by using the Ru–Ru₂P/V₂CT_x-based cathodic electrode paired with the anodic electrode based on RuO₂ catalyst, which is commonly employed for practical OER (inset of Fig. 5a). The Ru–Ru₂P/V₂CT_x(–)||RuO₂(+) system requires a low cell voltage of 1.47 or 1.72 V to reach current densities of 10 or 100 mA·cm^{–2}, respectively (Fig. 5a), which is much lower than the value required for the Pt/C(–)||RuO₂(+) system. To assess the industrial potential, the operation of the Ru–Ru₂P/V₂CT_x(–)||RuO₂(+) system at different temperatures was investigated in Fig. S40a. Very small cell voltage of only 1.46, 1.51, or 1.57 V is needed to achieve a current density of 50, 100, or 200 mA·cm^{–2}, respectively, at 75 °C, much better than its behavior at 50 or 25 °C (Fig. S40b). In addition, the stability test of the Ru–Ru₂P/V₂CT_x(–)||RuO₂(+) and Pt/C(–)||RuO₂(+) at 10 mA·cm^{–2} in Fig. 5b confirms that the Ru–Ru₂P/V₂CT_x(–)||RuO₂(+) can maintain steady activity over 100 h with a good retention of 92 %, whereas the Pt/C(–)||RuO₂(+) exhibits a quick degradation of activity with retention of only 75 % after 50 h operation. The LSV responses of the two electrolyzer systems also confirm the outstanding durability of the Ru–Ru₂P/V₂CT_x(–)||RuO₂(+) toward water splitting (Fig. S41). Furthermore, the Faradaic efficiency (η_F) of the Ru–Ru₂P/V₂CT_x(–)||RuO₂(+) measured at 20 mA·cm^{–2} (Fig. S42) is found to be approximately 96.4 % for the hydrogen evolution process (Fig. 5c). The Ru–Ru₂P/V₂CT_x(–)||RuO₂(+) electrolyzer even surpasses recently developed candidates derived from the MXene/Ru-based catalysts (Fig. 5d and Table S5). To verify practicability of the Ru–Ru₂P/V₂CT_x catalyst for water electrolysis, we established a single-cell AEMWE stack with the electrode couple of Ru–Ru₂P/V₂CT_x(–)||RuO₂(+) and an anion exchange membrane (Sustainion X37–50 Grade T) (Fig. 5e–f). The schematic illustration and photograph of AEMWE stack were shown in Fig. S43, Fig. S44 and Fig. S45. The current–voltage characteristic (*I*–*V*) of the Ru–Ru₂P/V₂CT_x(–)||RuO₂(+) AEMWE exhibits better performance, as compared to an AEMWE of the RuO_x/V₂CT_x(–)||RuO₂(+), V₂CT_x(–)||RuO₂(+), or even Pt/C(–)||RuO₂(+) (Fig. S46). Specifically, the Ru–Ru₂P/V₂CT_x(–)||RuO₂(+) AEMWE requires only 1.80 or 2.05 V to achieve a current density of 1.0 or 2.0 A·cm^{–2}, respectively (Fig. 5g), significantly smaller than that of the AEMWE derived from Pt/C(–)||RuO₂(+) (1.86 or 2.18 V), RuO_x/V₂CT_x(–)||RuO₂(+) (1.93 or 2.17 V), or V₂CT_x(–)||RuO₂(+) (2.28 or 2.60 V).

With a mass loading of precious active catalyst at cathode electrodes, such as Pt/C with Pt of 0.3 mg·cm^{–2} and Ru–Ru₂P/V₂CT_x with Ru of 0.36 mg·cm^{–2}, we estimate a precious metal cost of only US\$ 0.0058 cm^{–2} for Ru–Ru₂P/V₂CT_x-based cathodic electrode, better than that of the Pt/C. Furthermore, we also estimate a production cost of only US\$ 55.7 USD/g for Ru–Ru₂P/V₂CT_x catalyst-based electrode, significantly better than that of the commercial Pt/C-based electrode (156 USD/g), suggesting the highly practical promise of Ru–Ru₂P/V₂CT_x for industrial scale (Fig. S47). Durability of the Ru–Ru₂P/V₂CT_x(–)||RuO₂(+) stack was investigated at a current density of 0.5 A·cm^{–2} (Fig. 5h). Remarkably, the stack continuously operated for a period of 550 h with insignificant degradation rate of cell voltage approximate 72 μV·h^{–1}, evidencing the exceptional durability of Ru–Ru₂P/V₂CT_x HER electrode for long-term working conditions at an industrial scale. As a result, cell efficiency of the Ru–Ru₂P/V₂CT_x(–)||RuO₂(+) AEMWE is reduced only 2 % from 72.3 % to 70.3 % after 550 h testing. Energy efficiency of the Ru–Ru₂P/V₂CT_x is also found with high values of 68.33 % and 60.0 % to reach 1.0 and 2.0 A·cm^{–2}, respectively, corresponding to the energy consumption of 48.22 and 54.91 kWh·kg^{–1}H₂, respectively. Such achievements of the Ru–Ru₂P/V₂CT_x(–)||RuO₂(+) AEMWE also well surpass those of recently reported AEMWEs (Fig. 5i and Table S6). The

overall performances demonstrate the practical potential of Ru–Ru₂P/V₂CT_x catalyst towards high-efficiency HER in pH-universal environment for industrial-level water splitting application.

4. Conclusion

In summary, we report a heterostructure derived from Ru–Ru₂P clusters uniformly immobilized V₂CT_x nanosheets, which has been proven to be a superb HER electrocatalyst in a universal pH range, especially in universal-pH 0.5 M H₂SO₄ and 1.0 M KOH. The catalyst achieves low overpotentials of 37 and 21 mV at 10 mA·cm^{–2} with corresponding Tafel slopes of 61.3 and 31.4 mV·dec^{–1} in acidic and alkaline environments, respectively. The DFT calculations verify that the formation of Ru–Ru₂P/V₂CT_x interfaces leads to strong interaction between components to result in electronic reconfiguration and adjusted d-band centers, thus lowering the adsorption energy of hydrogen and facilitating the water dissociation. The constructed AEMWE device can achieve current densities of 1.0 and 2.0 A·cm^{–2} at cell voltage of 1.80 and 2.05 V, respectively, and excellent stability of over 550 h at 0.5 A·cm^{–2} with a degradation rate of only 72 μV·h^{–1}. This work fills the gap between the requirements of highly efficient and durable MXene-based electrocatalysts and the industrial demand for large-scale hydrogen production in the practical implementation of water electrolysis.

CRedit authorship contribution statement

Thanh Hai Nguyen: Methodology, Investigation, Validation, Formal analysis, Writing – original draft. **Phan Khanh Linh Tran:** Investigation, Validation, Formal analysis. **Duy Thanh Tran:** Conceptualization, Writing – review & editing, Supervision. **Van An Dinh:** Software, Validation, Formal analysis. **Nam Hoon Kim:** Visualization, Writing – review & editing, Supervision. **Joong Hee Lee:** Conceptualization, Writing – review & editing, Supervision.

Declaration of Competing Interest

The authors declare that they have no known competing financial interests or personal relationships that could have appeared to influence the work reported in this paper.

Data availability

Data will be made available on request.

Acknowledgements

This research was supported by the BRL (RS-2023-00207836) and the Regional Leading Research Center Program (2019R1A5A8080326) through the National Research Foundation funded by the Ministry of Science and ICT of the Republic of Korea.

Appendix A. Supporting information

Supplementary data associated with this article can be found in the online version at doi:10.1016/j.apcatb.2023.123517.

References

- [1] N. Du, C. Roy, R. Peach, M. Turnbull, S. Thiele, C. Bock, Anion-exchange membrane water electrolyzers, *Chem. Rev.* 122 (2022) 11830–11895.
- [2] Q. Xu, L. Zhang, J. Zhang, J. Wang, Y. Hu, H. Jiang, C. Li, Anion exchange membrane water electrolyzer: electrode design, lab-scaled testing system and performance evaluation, *EnergyChem* 4 (2022), 100087.
- [3] L. Gao, F. Bao, X. Tan, M. Li, Z. Shen, X. Chen, Z. Tang, W. Lai, Y. Lu, P. Huang, C. Ma, S.C. Smith, Z. Ye, Z. Hu, H. Huang, Engineering a local potassium cation concentrated microenvironment toward the ampere-level current density hydrogen evolution reaction, *Energy Environ. Sci.* 16 (2023) 285–294.

- [4] P.K.L. Tran, D.T. Tran, D. Malhotra, S. Prabhakaran, D.H. Kim, N.H. Kim, J.H. Lee, Highly effective freshwater and seawater electrolysis enabled by atomic Rh-modulated Co-CoO lateral heterostructures, *Small* 17 (2021), 2103826.
- [5] M. Islam, D.T. Tran, T.H. Nguyen, V.A. Dinh, N.H. Kim, J.H. Lee, Efficient synergism of NiO-NiSe₂ nanosheet-based heterostructures shelled titanium nitride array for robust overall water splitting, *J. Colloid Interface Sci.* 612 (2022) 121–131.
- [6] R. Subbaraman, D. Tripkovic, D. Strmcnik, K.-C. Chang, M. Uchiumura, A. P. Paulikas, V. Stamenkovic, N.M. Markovic, Enhancing hydrogen evolution activity in water splitting by tailoring Li+-Ni(OH)2-Pt interfaces, *Science* 334 (2011) 1256–1260.
- [7] X.-Z. Fan, Q.-Q. Pang, Recent research advances in ruthenium-based electrocatalysts for water electrolysis across the pH-Universal Conditions, *Energy Technol.* 10 (2022), 2200655.
- [8] C. Wang, L. Qi, Hollow nanosheet arrays assembled by ultrafine ruthenium-cobalt phosphide nanocrystals for exceptional pH-universal hydrogen evolution, *ACS Mater. Lett.* 3 (2021) 1695–1701.
- [9] Y. Zhao, X. Zhang, Y. Gao, Z. Chen, Z. Li, T. Ma, Z. Wu, L. Wang, S. Feng, Heterostructure of RuO₂-RuP₂/Ru derived from HMT-based coordination polymers as superior pH-universal electrocatalyst for hydrogen evolution reaction, *Small* 18 (2022), 2105168.
- [10] J. Zhang, Q. Zhang, X. Feng, Support and interface effects in water-splitting electrocatalysts, *Adv. Mater.* 31 (2019), 1808167.
- [11] X. Wang, Y. Tang, J.-M. Lee, G. Fu, Recent advances in rare-earth-based materials for electrocatalysis, *Chem. Catal.* 2 (2022) 967–1008.
- [12] D. Thanh Tran, T. Kshetri, N. Dinh Chuong, J. Gautam, H. Van Hien, L. Huu Tuan, N.H. Kim, J.H. Lee, Emerging core-shell nanostructured catalysts of transition metal encapsulated by two-dimensional carbon materials for electrochemical applications, *Nano Today* 22 (2018) 100–131.
- [13] D.T. Tran, D.C. Nguyen, H.T. Le, T. Kshetri, V.H. Hoa, T.L.L. Doan, N.H. Kim, J. H. Lee, Recent progress on single atom/sub-nano electrocatalysts for energy applications, *Prog. Mater. Sci.* 115 (2021), 100711.
- [14] C. Li, S.H. Kim, H.Y. Lim, Q. Sun, Y. Jiang, H.J. Noh, S.J. Kim, J. Baek, S.K. Kwak, J.B. Baek, Self-accommodation induced electronic metal-support interaction on ruthenium site for alkaline hydrogen evolution reaction, *Adv. Mater.* 35 (2023), 2301369.
- [15] A. VahidMohammadi, J. Rosen, Y. Gogotsi, The world of two-dimensional carbides and nitrides (MXenes), *Science* 372 (2021), eabf1581.
- [16] D. Sha, C. Lu, W. He, J. Ding, H. Zhang, Z. Bao, X. Cao, J. Fan, Y. Dou, L. Pan, Z. Sun, Surface selenization strategy for V₂CT_x MXene toward superior Zn-ion storage, *ACS Nano* 16 (2022) 2711–2720.
- [17] H.P. Li, X.R. Li, J.J. Liang, Y.S. Chen, Hydrous RuO₂-Decorated MXene coordinating with silver nanowire inks enabling fully printed micro-supercapacitors with extraordinary volumetric performance, *Adv. Energy Mater.* 9 (2019), 1803987.
- [18] T.H. Nguyen, P.K.L. Tran, V.A. Dinh, D.T. Tran, N.H. Kim, J.H. Lee, Metal single-site molecular complex-MXene Heteroelectrocatalysts Interspersed Graphene Nanonetwork for Efficient Dual-task of Water Splitting and Metal-air Batteries, *Adv. Funct. Mater.* 33 (2023), 2210101.
- [19] P.K.L. Tran, D.T. Tran, M. Austeria P, D.H. Kim, N.H. Kim, J.H. Lee, Intermolecular metallic single-site complexes dispersed on Mo₂TiC₂T_x/MoS₂ heterostructure induce boosted solar-driven water splitting, *Adv. Energy Mater.* 13 (2023), 2203844.
- [20] K. Matthews, T. Zhang, C.E. Shuck, A. VahidMohammadi, Y. Gogotsi, Guidelines for synthesis and processing of chemically stable two-dimensional V₂CT_x MXene, *Chem. Mater.* 34 (2022) 499–509.
- [21] H. Zhou, Z. Chen, A.V. López, E.D. López, E. Lam, A. Tsoukalou, E. Willinger, D. A. Kuznetsov, D. Mance, A. Kierzkowska, F. Donat, P.M. Abdala, A. Comas-Vives, C. Copéret, A. Fedorov, C.R. Müller, Engineering the Cu/Mo₂CT_x (MXene) interface to drive CO₂ hydrogenation to methanol, *Nat. Catal.* 4 (2021) 860–871.
- [22] Z. Wu, J. Shen, C. Li, C. Zhang, K. Feng, Z. Wang, X. Wang, D.M. Meira, M. Cai, D. Zhang, S. Wang, M. Chu, J. Chen, Y. Xi, L. Zhang, T.-K. Sham, A. Genest, G. Rupprechter, X. Zhang, L. He, Mo₂TiC₂ MXene-supported Ru clusters for efficient photothermal reverse water-gas shift, *ACS Nano* 17 (2023) 1550–1559.
- [23] L. Wang, L. Song, Z. Yang, Y.-M. Chang, F. Hu, L. Li, L. Li, H.-Y. Chen, S. Peng, Electronic modulation of metal-organic frameworks by interfacial bridging for efficient pH-universal hydrogen evolution, *Adv. Funct. Mater.* 33 (2023), 2210322.
- [24] L. Wang, Y. Hao, L. Deng, F. Hu, S. Zhao, L. Li, S. Peng, Rapid complete reconfiguration induced actual active species for industrial hydrogen evolution reaction, *Nat. Commun.* 13 (2022), 5785.
- [25] A. Kong, M. Peng, H. Gu, S. Zhao, Y. Lv, M. Liu, Y. Sun, S. Dai, Y. Fu, J. Zhang, W. Li, Synergetic control of Ru/MXene 3D electrode with superhydrophilicity and superaerophobicity for overall water splitting, *Chem. Eng. J.* 426 (2021), 131234.
- [26] V. Ramalingam, P. Varadhan, H.-C. Fu, H. Kim, D. Zhang, S. Chen, L. Song, D. Ma, Y. Wang, H.N. Alshareef, J.-H. He, Heteroatom-mediated interactions between ruthenium single atoms and an MXene support for efficient hydrogen evolution, *Adv. Mater.* 31 (2019), 1903841.
- [27] Y. Gogotsi, B. Anasori, The rise of MXenes, *ACS Nano* 13 (2019) 8491–8494.
- [28] D. Mohapatra, Y. Shin, M.Z. Ansari, Y.-H. Kim, Y.J. Park, T. Cheon, H. Kim, J. W. Lee, S.-H. Kim, Process Controlled Ruthenium on 2D engineered V-MXene via atomic layer deposition for human healthcare monitoring, *Adv. Sci.* 10 (2023), 2206355.
- [29] Y. Chen, H. Yao, F. Kong, H. Tian, G. Meng, S. Wang, X. Mao, X. Cui, X. Hou, J. Shi, V₂C MXene synergistically coupling FeNi LDH nanosheets for boosting oxygen evolution reaction, *Appl. Catal. B Environ.* 297 (2021), 120474.
- [30] S. Park, Y.-L. Lee, Y. Yoon, S.Y. Park, S. Yim, W. Song, S. Myung, K.-S. Lee, H. Chang, S.S. Lee, K.-S. An, Reducing the high hydrogen binding strength of vanadium carbide MXene with atomic Pt confinement for high activity toward HER, *Appl. Catal. B Environ.* 304 (2022), 120989.
- [31] X. Jin, H. Jang, N. Jarulertwathana, M.G. Kim, S.J. Hwang, Atomically thin holey two-dimensional ru₂p nanosheets for enhanced hydrogen evolution electrocatalysis, *ACS Nano* 16 (2022) 16452–16461.
- [32] F. Chen, B. Zhao, M. Sun, C. Liu, Y. Shi, Y. Yu, B. Zhang, Mechanistic insight into the controlled synthesis of metal phosphide catalysts from annealing of metal oxides with sodium hypophosphite, *Nano Res.* 15 (2022) 10134–10141.
- [33] Y.F. Chen, H.L. Yao, F.T. Kong, H. Tian, G. Meng, S.Z. Wang, X.P. Mao, X.Z. Cui, X. M. Hou, J.L. Shi, V₂C MXene synergistically coupling FeNi LDH nanosheets for boosting oxygen evolution reaction, *Appl. Catal. B Environ.* 297 (2021), 120474.
- [34] H. Wu, M. Almalki, X. Xu, Y. Lei, F. Ming, A. Mallick, V. Roddatis, S. Lopatin, O. Shekha, M. Eddaoudi, H.N. Alshareef, MXene derived metal-organic frameworks, *J. Am. Chem. Soc.* 141 (2019) 20037–20042.
- [35] A. VahidMohammadi, A. Hadjikhani, S. Shahbazmohamadi, M. Beidaghi, Two-dimensional vanadium carbide (MXene) as a high-capacity cathode material for rechargeable aluminum batteries, *ACS Nano* 11 (2017) 11135–11144.
- [36] C.W. Tung, T.R. Kuo, Y.P. Huang, Y.C. Chu, C.H. Hou, Y. Li, N.T. Suen, J. Han, H. M. Chen, Dynamic Co(μ-O)₂Ru moiety endowed efficiently catalytic hydrogen evolution, *Energy Mater.* 12 (2022), 2200079.
- [37] L. Qin, S.Y. Xu, Y. Liu, S.H. Zhu, L.R. Hou, C.Z. Yuan, Facile hydrothermal construction of Nb₂CT_x/Nb₂O₅ as A Hybrid Anode Material for High-performance Li-ion batteries, *Chin. Chem. Lett.* 31 (2020) 1030–1033.
- [38] C.F. Zhang, S.J. Kim, M. Ghidui, M.Q. Zhao, M.W. Barsoum, V. Nicolosi, Y. Gogotsi, Layered orthorhombic Nb₂O₅@Nb₄C₃T_x and TiO₂@Ti₃C₂T_x hierarchical composites for high performance Li-ion batteries, *Adv. Funct. Mater.* 26 (2016) 4143–4151.
- [39] A. Champagne, L. Shi, T. Ouisse, B. Hackens, J.-C. Charlier, Electronic and vibrational properties of V₂C-based MXenes: from experiments to first-principles modeling, *Phys. Rev. B* 97 (2018), 115439.
- [40] Y. Wang, J. Song, W.Y. Wong, Constructing 2D Sandwich-like MOF/MXene heterostructures for durable and fast aqueous zinc-ion batteries, *Angew. Chem. Int. Ed.* 62 (2023), e202218343.
- [41] C.E. Park, G.H. Jeong, J. Theerthagiri, H. Lee, M.Y. Choi, Moving beyond Ti₂C₃T_x MXene to Pt-decorated TiO₂@TiC core-shell via pulsed laser in reshaping modification for accelerating hydrogen evolution kinetics, *ACS Nano* 17 (2023) 7539–7549.
- [42] L. Deng, F. Hu, M. Ma, S.C. Huang, Y. Xiong, H.Y. Chen, L. Li, S. Peng, Electronic modulation caused by interfacial Ni-O-M (M= Ru, Ir, Pd) bonding for accelerating hydrogen evolution kinetics, *Angew. Chem., Int. Ed.* 60 (2021) 22276–22282.
- [43] P. Xiong, X. Zhang, H. Wan, S. Wang, Y. Zhao, J. Zhang, D. Zhou, W. Gao, R. Ma, T. Sasaki, G. Wang, Interface modulation of two-dimensional superlattices for efficient overall water splitting, *Nano Lett.* 19 (2019) 4518–4526.
- [44] Z.Q. Liu, X. Liang, F.X. Ma, Y.X. Xiong, G. Zhang, G. Chen, L. Zhen, C.Y. Xu, Decoration of NiFe-LDH nanodots endows lower Fe-d band center of Fe₁-N-C hollow nanorods as bifunctional oxygen electrocatalysts with small overpotential gap, *Adv. Energy Mater.* 13 (2023), 2203609.
- [45] Q. Yu, W. Yu, Y. Wang, J. He, Y. Chen, H. Yuan, R. Liu, J. Wang, S. Liu, J. Yu, H. Liu, W. Zhou, Hydroxyapatite-derived heterogeneous Ru-Ru₂P electrocatalyst and environmentally-friendly membrane electrode toward efficient alkaline electrolyzer, *Small* 19 (2023), 2208045.
- [46] G.Z. Li, T. Sun, H.J. Niu, Y. Yan, T. Liu, S.S. Jiang, Q.L. Yang, W. Zhou, L. Guo, Triple interface optimization of ru-based electrocatalyst with enhanced activity and stability for hydrogen evolution reaction, *Adv. Funct. Mater.* 33 (2023), 2212514.
- [47] Q. Liang, Q. Li, L. Xie, H. Zeng, S. Zhou, Y. Huang, M. Yan, X. Zhang, T. Liu, J. Zeng, K. Liang, O. Terasaki, D. Zhao, L. Jiang, B. Kong, Superassembly of surface-enriched Ru nanoclusters from trapping-bonding strategy for efficient hydrogen evolution, *ACS Nano* 16 (2022) 7993–8004.
- [48] D. Chen, R.H. Yu, R.H. Lu, Z.H. Pu, P.Y. Wang, J.W. Zhu, P.X. Ji, D.L. Wu, J.S. Wu, Y. Zhao, Z.K. Kou, J. Yu, S.C. Mu, Tunable Ru-Ru₂P heterostructures with charge redistribution for efficient pH-universal hydrogen evolution, *Infomat* 4 (2022), e12287.
- [49] J. Wang, Z.Z. Wei, S.J. Mao, H.R. Li, Y. Wang, Highly uniform Ru nanoparticles over N-doped carbon: pH and temperature-universal hydrogen release from water reduction, *Energy Environ. Sci.* 11 (2018) 800–806.
- [50] C. Yang, W. Zhong, K. Shen, Q. Zhang, R. Zhao, H. Xiang, J. Wu, X. Li, N. Yang, Electrochemically reconstructed Cu-FeOOH/Fe₃O₄ catalyst for efficient hydrogen evolution in alkaline media, *Adv. Energy Mater.* 12 (2022), 2200077.
- [51] H. Tan, B. Tang, Y. Lu, Q. Ji, L. Lv, H. Duan, N. Li, Y. Wang, S. Feng, Z. Li, C. Wang, F. Hu, Z. Sun, W. Yan, Engineering a local acid-like environment in alkaline medium for efficient hydrogen evolution reaction, *Nat. Commun.* 13 (2022), 2024.
- [52] M. Lao, P. Li, Y. Jiang, H. Pan, S.X. Dou, W. Sun, From fundamentals and theories to heterostructured electrocatalyst design: an in-depth understanding of alkaline hydrogen evolution reaction, *Nano Energy* 98 (2022), 107231.
- [53] P. Yan, T. Yang, M. Lin, Y. Guo, Z. Qi, Q. Luo, X.Y. Yu, “One Stone Five Birds” plasma activation strategy synergistic with Ru single atoms doping boosting the hydrogen evolution performance of metal hydroxide, *Adv. Funct. Mater.* (2023), 2301343.
- [54] Q. Du, E. Freysz, Y.R. Shen, Vibrational spectra of water molecules at quartz/water interfaces, *Phys. Rev. Lett.* 72 (1994) 238–241.
- [55] J.-J. Velasco-Velez, C.H. Wu, T.A. Pascal, L.F. Wan, J. Guo, D. Prendergast, M. Salmeron, The structure of interfacial water on gold electrodes studied by x-ray absorption spectroscopy, *Science* 346 (2014) 831–834.

- [56] K. Wang, J. Cao, X. Yang, X. Sang, S. Yao, R. Xiang, B. Yang, Z. Li, T. O'Carroll, Q. Zhang, L. Lei, G. Wu, Y. Hou, Kinetically accelerating elementary steps via bridged Ru-H state for the hydrogen-evolution in anion-exchange membrane electrolyzer, *Adv. Funct. Mater.* 33 (2023), 2212321.
- [57] R. Gao, J. Wang, Z.-F. Huang, R. Zhang, W. Wang, L. Pan, J. Zhang, W. Zhu, X. Zhang, C. Shi, J. Lim, J.-J. Zou, Pt/Fe₂O₃ with Pt-Fe pair sites as a catalyst for oxygen reduction with ultralow Pt loading, *Nat. Energy* 6 (2021) 614–623.
- [58] J.X. Wei, K. Xiao, Y.X. Chen, X.P. Guo, B.L. Huang, Z.Q. Liu, In situ precise anchoring of Pt single atoms in spinel Mn₃O₄ for a highly efficient hydrogen evolution reaction, *Energy Environ. Sci.* 15 (2022) 4592–4600.
- [59] J.K. Nørskov, F. Abild-Pedersen, F. Studt, T. Bligaard, Density functional theory in surface chemistry and catalysis, *Proc. Natl. Acad. Sci. USA* 108 (2011) 937–943.
- [60] Q. Hu, K. Gao, X. Wang, H. Zheng, J. Cao, L. Mi, Q. Huo, H. Yang, J. Liu, C. He, Subnanometric Ru clusters with upshifted d band center improve performance for alkaline hydrogen evolution reaction, *Nat. Commun.* 13 (2022), 3958.
- [61] J.K. Nørskov, T. Bligaard, A. Logadottir, J.R. Kitchin, J.G. Chen, S. Pandalov, U. Stimming, Trends in the exchange current for hydrogen evolution, *J. Electrochem. Soc.* 152 (2005) J23.
- [62] J.X. Shen, R.L. Fan, Y.J. Wang, J. Zhou, C. Chen, Z.H. Wei, S. Ju, T. Qian, Y. Peng, M.R. Shen, Oxygen-vacancy-rich nickel hydroxide nanosheet: a multifunctional layer between Ir and Si toward enhanced solar hydrogen production in alkaline media, *Energy Environ. Sci.* 15 (2022) 3051–3061.